Lawrence Berkeley National Laboratory

Title
Infrared-active optical phonons in LiFePO4 single crystals

Permalink
https://escholarship.org/uc/item/43h8x73b

Authors
Stanislavchuk, TN
Middlemiss, DS
Syzdek, JS
et al.

Peer reviewed

Infrared-active optical phonons in LiFePO$_4$ single crystals

T. N. Stanislavchuk,[1,*] Derek S. Middlemiss,[2] Jaroslaw Syzdek,[3] Yuri Janssen,[4] R. Basistyy,[1] A. A. Sirenko,[1] Peter Khalifah,[4,5] Clare P. Grey[2] and Robert Kostecki[3]

^{1}Department of Physics, New Jersey Institute of Technology, Newark, New Jersey 07102, USA

^{2}Department of Chemistry, University of Cambridge, Cambridge, UK, CB2 1EW

^{3}Lawrence Berkeley National Laboratory, 94720 CA, USA

^{4}Department of Chemistry, Stony Brook University, Stony Brook 11790 NY, USA

^{5}Chemistry Department, Brookhaven National Laboratory, Upton 11763 NY, USA

Abstract

Infrared-active optical phonons were studied in olivine LiFePO$_4$ oriented single crystals by means of both rotating analyzer and rotating compensator spectroscopic ellipsometry in the spectral range between 50 and 1400 cm^{-1}. The eigenfrequencies, oscillator strengths and broadenings of the phonon modes were determined from fits of the anisotropic harmonic oscillator model to the data. Optical phonons in a heterosite FePO$_4$ crystal were measured from the delithiated *ab*-surface of the LiFePO$_4$ crystal and compared with the phonon modes of the latter. Good agreement was found between experimental data and the results of solid-state hybrid density functional theory calculations for the phonon modes in both LiFePO$_4$ and FePO$_4$.

* Author to whom correspondence should be addressed. Electronic mail: stantar@njit.edu

1

I. INTRODUCTION

Olivine lithium iron phosphate LiFePO$_4$ (LFP) has attracted considerable attention as one of the most promising materials for cathodes in Li-ion rechargeable batteries since its first introduction in this role by Padhi *et al.* [1]. The great interest in LFP can be attributed to its flat discharge voltage of 3.4 V *vs.* Li$^+$/Li, significant theoretical capacity of 170 mAh/g, high thermal stability, and environmental sustainability [2,3,4]. At the same time, the low electronic and ionic conductivities of LFP result in low cycling capacity at high discharge rate, preventing the effective use of these materials in Li batteries [5,6]. It is known that electrochemical insertion or removal of Li$^+$ ions proceeds via a first order transformation between LFP and heterosite FePO$_4$ (FP) phases [1,3]. The precise mechanism of the intercalation process is not well understood [7]. The discussed models include: (i) the core-shell model, where the center of the crystal is FP and the periphery is LFP during both the charging and discharging processes [1,8]; (ii) nucleation growth models, where the new phase is first nucleated and then propagates through the crystal [9,10]; and (iii) the single phase model, where Li$_x$FePO$_4$ is preserved throughout the range $0 \leq x \leq 1$ [11]. Vibrational spectroscopies such as infrared (IR) and Raman are sensitive to Li concentration in the Li$_x$FePO$_4$ phase and can provide additional information on the intercalation process. Indeed, insertion or removal of Li ions changes the crystal field environment of the oxygen anions coordinated to the Li sites in the solid and thus influences the vibrational properties of the lattice. Furthermore, the diffusion rate of Li ions depends upon the vibrations of the lattice (phonons) and the potential minima encountered along the diffusion pathways of the cathode material [12]. Recent advances in IR near-field microscopy allow for the study of chemical composition of Li$_x$FePO$_4$ specimens at the submicron scale when the atomic force microscope tip is illuminated with light at frequencies in resonance with the phonon modes of a specimen [13]. Thus, a knowledge of the phonon modes of Li$_x$FePO$_4$ ($0 \leq x \leq 1$) crystals is important for a correct understanding of (de)intercalation processes.

The *Pnma* structure of LiFePO$_4$ contains four formula units (28 atoms) per unit cell. As a result LiFePO$_4$ possesses 84 normal vibrations, among which 38 are IR active modes ($14B_{1u} + 10B_{2u} + 14B_{3u}$), one of each of which is acoustic, and 36 are Raman active modes ($11A_g + 7B_{1g} + 11B_{2g} + 7B_{3g}$). Optical phonon spectra at the Brillouin zone center have to date been measured only in polycrystalline samples by IR [14,15] and Raman spectroscopies [14,15,16,17], and calculated by various theoretical methods [13,18,19,20]. Parques-Ledent and Tarte

[14] performed a thorough analysis of IR and Raman modes of LFP polycrystalline samples, including isotopic studies with [6]Li-[7]Li substitution. They demonstrated that the LFP phonon modes are spectrally separated into two bands: the high frequency band above 750 cm^{-1} corresponds to internal stretching modes of PO_4 anion groups, while the mid-to-low frequency band below 750 cm^{-1} corresponds to internal bending modes of PO_4 groups combined with external modes such as rotations and translations. Isotopic shifts were registered for a number of IR modes providing insight into their relationship with Li ion motions. Further investigations of the phonon spectra of Li_xFePO_4 as a function of Li concentration ($0 \leq x \leq 1$) was carried out by Burba and Frech [15]. In particular, they showed that the intramolecular PO_4 modes are especially sensitive to Li extraction from LFP.

While spectroscopic measurements on polycrystalline samples has helped establish the general pattern of phonon modes in Li_xFePO_4 compounds, an accurate determination of the parameters of the phonon modes, such as symmetry, frequency, oscillator strength and broadening, can be achieved only by measurements on oriented single crystals. So far such measurements have been hindered mainly by the small sizes of available samples. Here we present our IR data for large single crystals of $LiFePO_4$ measured along all three principal crystallographic directions by means of both rotating analyzer and rotating compensator spectroscopic ellipsometry. Although $FePO_4$ crystals were not available in the bulk form, we carried out ellipsometric measurements on the *ab*-plane of a $LiFePO_4$ sample treated with bromine solution to chemically extract Li ions from the surface of the sample, thus enabling IR measurements of a $FePO_4$ crystal. For the purpose of the ellipsometric measurements such delithiated samples were equivalent to thick films of $FePO_4$ on top of $LiFePO_4$ substrate such that the film thickness was greater than the penetration depth of light. The ellipsometric measurements were complemented with solid-state hybrid density functional theory (DFT) calculations of the phonon modes, yielding phonon parameters in a good agreement with the experimental data.

II. EXPERIMENTAL AND THEORETICAL TECHNIQUES

A. Sample growth and preparation

Low-defect $LiFePO_4$ single crystals were grown by flux growth techniques, using Li_3PO_4, LiCl, and $FeCl_2$ as reagents, as described in detail in Ref.[21]. The selected crystals were

~ 5×5×4 mm^3 in size and of a good optical quality. Crystals were oriented using a Bruker Kappa Apex II X-ray diffractometer prior to cutting and polishing them perpendicular to the *a* and *c* axes for the optical measurements.

To study optical properties of FePO$_4$ samples, LiFePO$_4$ crystals were treated with a solution of bromine in acetonitrile (Br$_2$/CH$_3$CN) to chemically extract Li ions from the near-surface layers of the samples. In order to evaluate the efficiency of the delithiation process scanning electron microscopy (SEM) images of chemically delithiated LiFePO$_4$ single crystals were obtained using JEOL FESEM7500F microscope. These investigations showed vastly different reactivity of different crystal facets, with some being virtually unaffected by the treatment, and other facets undergoing either mild cracking with ~200-300nm spacing, and some chipping completely off. Interestingly, the contact angle of the bromine solution and the crystal (i.e. the wetting properties) also depended strongly on the facet. In general, the facets that underwent delithiation exhibited large contact angles (>90 degrees) and those that did not, were well-wetted.

B. Ellipsometry technique

The rotating analyzer ellipsometry (RAE) and rotating compensator ellipsometry (RCE) measurements were carried out on the U4IR beamline of the National Synchrotron Light Source (NSLS) at Brookhaven National Laboratory (BNL). The ellipsometry setup, described in detail in Refs. [22,23], allowed us to measure the optical phonon spectra in the range between 50 and 2000 cm^{-1} with a spectral resolution of 0.7 cm^{-1}. All measurements described in this paper were taken at room temperature. The ellipsometer setup at the U4IR beamline consists of a Bruker v66i spectrometer equipped with beamsplitters and detectors for different spectral ranges, and two corresponding sets of linear polarizers and optical retarders. For the spectral range below 500 cm^{-1} we used a LHe 4 K bolometer, a Ge-Mylar beamsplitter, polyethylene wire grid linear polarizers, and Si retarders. A LHe-cooled CuGe detector, a KBr beamsplitter, and KRS5 wire grid linear polarizers were used for the spectral range between 400 cm^{-1} and 2000 cm^{-1}. In this paper, our main interest is in the optical phonons between 100 cm^{-1} and 1200 cm^{-1}, so both sets of optical elements were necessary. A significant overlap between the two spectral ranges allowed for a smooth merge of the measured optical spectra in the region from 400 to 500 cm^{-1}. The angle of incidence (AOI) of the light upon the sample was 75° for all ellipsometric

measurements, a value close to the Brewster angle of ~70° for the low-frequency spectral range of LiFePO$_4$. In what follows, we use a standard ellipsometry convention for the Cartesian x, y, z coordinate system: z is perpendicular to the reflecting surface of the sample, x is parallel and y is, correspondingly, perpendicular to the reflection plane.

The main advantage of ellipsometry in comparison with conventional reflectivity measurements is the possibility to measure both real and imaginary parts of the *pseudo*-dielectric function $\langle \varepsilon(\omega) \rangle$. In RAE the spectra $\langle \varepsilon(\omega) \rangle$ are related to AOI and measurable ellipsometric angles $\Psi(\omega)$ and $\Delta(\omega)$ as follows:

$$\langle \varepsilon(\omega) \rangle = \sin^2 \theta + \sin^2 \theta \cdot \tan^2 \theta \cdot \left[\frac{1 - \tan \Psi(\omega) \cdot e^{i\Delta(\omega)}}{1 + \tan \Psi(\omega) \cdot e^{i\Delta(\omega)}} \right]^2, \qquad (1)$$

where $\tan \Psi(\omega) = |r_p(\omega) / r_s(\omega)|$ is the ratio of Fresnel's coefficients or reflection amplitudes, $\Delta(\omega) = \delta_p(\omega) - \delta_s(\omega)$ is the phase difference between s- and p-polarized light, and θ represents the AOI. Note here that RAE can measure only $\cos(\Delta)$, while the $\sin(\Delta)$ remains undetermined.

RCE is known to be more robust than RAE due to a better stability against experimental errors caused by depolarization of reflected light and back-side reflection from the measured samples. The latter is significant only in the transparency spectral range at low frequencies, i. e., below the optical phonon frequencies. RCE also has a powerful experimental capability to measure both $\cos(\Delta)$ and $\sin(\Delta)$, which results in simultaneous measurement of several additional non-trivial components of the 4×4 Mueller matrix (MM) of the sample; the latter connects the Stokes polarization vectors for incoming $\vec{S}_{IN}$ and outgoing $\vec{S}_{OUT}$ reflected light. In contrast to full MM ellipsometry, RCE permits for the measurement of a truncated 4×3 Mueller matrix with nontrivial components M_{21}, M_{33}, and M_{43}. For each frequency ω of the measured spectra, the Mueller matrix $\hat{M}(\omega)$ is defined as $\vec{S}_{OUT}(\omega) = \hat{M}(\omega) \cdot \vec{S}_{IN}(\omega)$. In the following, the

experimental data for RCE will be presented in terms of the *normalized* Mueller matrix components $m_{ij}(\omega) = M_{ij}(\omega) / M_{11}(\omega)$ that are even more robust against systematic experimental errors than $M_{11}(\omega)$ due to self-normalization by the total reflectivity given by the $M_{11}(\omega)$ spectrum. The measured experimental spectra $m_{ij}(\omega)$, which vary from -1 to $+1$, are related to the model parameters for an anisotropic dielectric function $\varepsilon(\omega)$ via analytical formulas that are well known and presented in Ref. [24].

C. Density functional theory calculations

Calculations of the Brillouin zone center (Γ-point) phonon frequencies, mode displacement patterns and oscillator strengths for bulk $LiFePO_4$ and $FePO_4$ were performed within the CRYSTAL09 linear combinations of atomic orbitals code [25,26]. The basis sets used comprise a series of atom-centered Gaussian primitive functions grouped into contractions of the form (7s,2p,1d) / [1s,2sp,1d] for Li; (10s,4p,1d) / [1s,2sp,1d] for O; (16s,8p,1d) / [1s,3sp,1d] for P; and (20s,12p,5d) / [1s,4sp,2d] for Fe, where the values in parentheses denote the number of Gaussian primitives, and the values in square brackets denote the contraction scheme. The basis sets were taken from the CRYSTAL09 online repository, and were unmodified from their use in a wide range of materials bearing similar site charges [27]. The hybrid B3LYP exchange-correlation functional was used throughout [28,29,30]. Prior to commencing the phonon calculations, the crystal structures of $LiFePO_4$ and $FePO_4$ were fully optimized using convergence tolerances of 10^{-10} atomic units (AU) for total energy, 5×10^{-6} AU for root mean square (RMS) atomic gradient and 2×10^{-5} AU for RMS atomic displacement. The *Pnma* space group symmetry of the primitive cells was enforced throughout both structural optimizations, and ferromagnetic alignments of the unpaired Fe spin moments were assumed in all cases. Note that no significant effects upon the phonon parameters are expected due to ordering of the Fe^{2+} magnetic moments, given that antiferromagnetism appears only at low temperatures below $T_N = 50$ K in this material [31]. To show the dependence of computed phonon properties on cell volume, phonon calculations on both materials were also performed using fixed experimental cells (with fully optimized atomic positions) obtained from neutron diffraction at 300 K [32]. Reciprocal space was sampled upon Monkhorst-Pack meshes with shrinking factors $4 \times 8 \times 8$ for

both phases, yielding 75 **k**-points in the irreducible Brillouin zone. Phonon calculations proceeded within the finite atomic displacement approach using a central difference method to compute the first derivatives of the atomic gradients [33,34]. Atomic displacements of magnitude 0.005 AU along the Cartesian directions were used. Tests with varying displacement magnitudes yielded no significant variation in phonon properties. The crystal symmetry of the unperturbed lattice was used throughout to assist in filling the force constants matrix. The oscillator strengths were obtained via calculations of the atomic dynamical charge tensors [35] within a Wannier-Boys localization approach [36]. The mode atomic displacement patterns were analyzed by means of a building unit decomposition, which provides a systematic classification of the modes in terms of the external (rigid unit motions) and internal (unit distortive motions) contributions of LiO_6, FeO_6 and PO_4 units, as appropriate.

III. RESULTS AND DISCUSSION

A. Phonon modes of $LiFePO_4$

Figure 1(a-i) shows normalized spectra of the Mueller matrix components $m_{12}(\omega)$, $m_{33}(\omega)$, and $m_{43}(\omega)$ (blue curves) for $LiFePO_4$ crystals measured using RCE at T=300 K for three different sample orientations with respect to the experimental setup: $a \parallel x$ and $b \parallel y$; $b \parallel x$ and $a \parallel y$; and $c \parallel x$ and $b \parallel y$. The strong sharp features in the spectra correspond to transverse optical (TO) phonons. Due to relatively high values of the dielectric constant at the resonance with phonons and the proximity of the AOI=75° to the Brewster angle, the main contributions to each spectrum originate primarily from the TO phonons that are polarized along the x-direction for each experimental configuration. Thus, to determine the optical phonon frequencies for all three crystallographic axes a, b, and c, one needs at least three measurements with $a \parallel x$, $b \parallel x$, and $c \parallel x$, exactly as shown in Figure 1. In addition to the primary contribution from the TO phonons polarized along x, the Mueller matrix spectra also contain features originating from the *reststrahlen* bands in the proximity of the LO phonon frequencies that are polarized along the y and z directions.

The Mueller matrix representation for the experimental optical phonon spectra is not conventional in the condensed matter community. A more common way to present experimental data is via a *pseudo*-dielectric function $\langle \varepsilon(\omega) \rangle$. In the case of an isotropic bulk sample, $\langle \varepsilon(\omega) \rangle$

7

would coincide with the dielectric function, but for strongly anisotropic samples such as LiFePO$_4$, $\langle \varepsilon(\omega) \rangle$ depends on the AOI and contains contributions from phonons polarized along all three crystallographic axes, a, b, and c. Still, for the same reasons as outlined above for the Mueller matrix spectra, each spectrum of $\langle \varepsilon(\omega) \rangle$ has a dominant contribution from the phonons polarized along the corresponding x axis. Figure 2(a-c) shows experimental spectra of $\langle \varepsilon(\omega) \rangle$ measured for three experimental configurations with $a \parallel x$, $b \parallel x$, and $c \parallel x$. The low-frequency part of the $\langle \varepsilon(\omega) \rangle$ spectra in Fig. 2 (below 450 cm^{-1}) has been directly converted from the experimental Mueller matrix spectra $m_{ij}(\omega)$ shown in Fig. 1. The high-frequency part of the $\langle \varepsilon(\omega) \rangle$ spectra in Fig. 2 (above 450 cm^{-1}) has been obtained from RAE measurements [see Eq. (1)]. The *reststrahlen* bands result in unusual spectral features with negative values of pseudo $\langle \varepsilon_2(\omega) \rangle$ and inverted Lorentz oscillator forms in $\langle \varepsilon_1(\omega) \rangle$, as can be seen, for example, at ~1100 cm^{-1} in Figs. 2(a) and 2(c).

The difference between the RAE and RCE ellipsometry measurements is illustrated in Fig. 3(a,b) where we show a comparison between real and imaginary parts obtained with these two realizations of the ellipsometry technique. For the high-frequency part ($\omega > 230$ cm^{-1}) both approaches return similar spectra, while for the low-frequency part ($\omega < 230$ cm^{-1}) the differences are more notable: the real part $\langle \varepsilon_1(\omega) \rangle$ is lower and the imaginary part $\langle \varepsilon_2(\omega) \rangle$ is significantly higher in RAE than in RCE spectra. We note that the broad background in $\langle \varepsilon_2(\omega) \rangle$ in the low-frequency part of the spectrum, being essentially constant at approximately 10, is not physical because our samples are known to be transparent at frequencies sufficiently far below the lowest phonon mode. This systematic error in the RAE measurements is due to several factors, such as sample diffuse scattering, back-side reflection, and detector dark-current contributions to the measured intensities. From the formal point of view, the quality of RAE data at low frequencies is affected by proximity of $\Delta(\omega)$ to zero, which automatically enhances all systematic errors of the measurements. In RCE measurements most of the aforementioned systematic errors are automatically eliminated due to the presence of higher order Fourier coefficients in the standard ellipsometry data conversion. Note again that all of our phonon data at $\omega < 500$ cm^{-1} were obtained from RCE spectra. An additional difference

between RAE and RCE can be seen for the sharp feature at ~ 200 cm^{-1} marked with a star in Figure 3(a,b). This peak originates from the *reststrahlen* bands of two phonons at ~ 200 cm^{-1} polarized along the *b* and *c*-axes. The phase $\Delta(\omega)$ would require careful consideration in such a non-trivial situation featuring an anisotropic dielectric function, and can be properly treated only via advanced simulation tools of the type described below.

To decouple the dielectric contributions along *x* and *z* in each measurement, we fit the experimental RCE spectra $m_{12}(\omega)$, $m_{33}(\omega)$, and $m_{43}(\omega)$, as well as the RAE spectra $\langle\varepsilon(\omega)\rangle$, using an anisotropic dielectric function model for $\hat{\varepsilon}(\omega)$:

$$\hat{\varepsilon}(\omega) = \begin{bmatrix} \varepsilon_a(\omega) & 0 & 0 \\ 0 & \varepsilon_b(\omega) & 0 \\ 0 & 0 & \varepsilon_c(\omega) \end{bmatrix}$$

$$\varepsilon_a(\omega) = \varepsilon_{\infty,a} + \sum_{k=1}^{K} \frac{S_k \cdot \omega_k^2}{\omega_k^2 - \omega^2 - i\gamma_k\omega},$$

$$\varepsilon_b(\omega) = \varepsilon_{\infty,b} + \sum_{l=1}^{L} \frac{S_l \cdot \omega_l^2}{\omega_l^2 - \omega^2 - i\gamma_l\omega}, \qquad (2)$$

$$\varepsilon_c(\omega) = \varepsilon_{\infty,c} + \sum_{n=1}^{N} \frac{S_n \cdot \omega_n^2}{\omega_n^2 - \omega^2 - i\gamma_n\omega}.$$

Here the contribution of phonons polarized along the *a(b,c)* axis to the corresponding diagonal component $\varepsilon_{a(b,c)}(\omega)$ of the dielectric function tensor is described by a set of Lorentz oscillators, where $\omega_{k(l,n)}$ is the TO phonon frequency, $S_{k(l,n)}$ is the phonon oscillator strength, and $\gamma_{k(l,n)}$ is the phonon broadening; $\varepsilon_{\infty,a(b,c)}$ represents the dielectric constant at frequencies above the optical phonons ($\omega > 1300$ cm^{-1}). As was pointed above, the main contribution to each spectrum $\langle\varepsilon(\omega)\rangle$ originates from the TO phonons that are polarized along the *x*-direction of the experimental configuration. From visual inspection of the measured spectra we were able to identify *K*=11, *L*=9, and *N*=12 TO phonon modes polarized along the *a*, *b*, and *c* axes, respectively and, as a result, construct initial set of Lorentz oscillators for the model. A locally written program based on the 4×4 Berreman matrix propagation method for anisotropic magneto-electric media was used to fit the model to the experimental data.[37] The results of the fit are shown by red dotted curves in Figs. 1(a-i) and 2(a-c). It is clear that the Berreman method provides an accurate

9

description of most of the negative features in the $\langle \varepsilon_2(\omega) \rangle$ spectra, indicating that the phase of the reflected light [or, equivalently, $\sin \Delta(\omega)$] has been calculated correctly even for the *reststrahlen* bands.

Table I summarizes the experimental values for parameters of the TO phonons for all three orthorhombic cell axes *a*, *b*, and *c*. There are total of 32 TO phonons listed in Table I (*K*=11, *L*=9, and *N*=12). The number of phonons predicted for the *Pnma* symmetry cell of LiFePO$_4$ is 35 (*K*=13, *L*=9 and *N*=13). So it is possible that some weak phonons with oscillator strengths less than approximately 0.02 cannot be resolved by these measurements due to a complicated optical response of the anisotropic crystal, particularly in a situation where a weak phonon polarized along one axis falls close in frequency to a separate strong phonon polarized along an orthogonal axis. The $\varepsilon_{\infty,a(b,c)}$ values, which are determined by high energy electronic transitions, are 2.8±0.1 for all three *a*, *b*, and *c* axes (see Table I). The combined contribution of the oscillator strengths of the optical phonons and $\varepsilon_{\infty,a(b,c)}$ result in the low-frequency (THz spectral range) values of $\varepsilon_a(0) = 8.1$, $\varepsilon_b(0) = 7.3$ and $\varepsilon_c(0) = 7.6$ for *a*, *b*, and *c* axes correspondingly (see Table I).

Figure 4 shows anisotropic dielectric function model for LiFePO$_4$ crystals calculated using the fit parameters from Table I for tensor components $\varepsilon_a(\omega)$, $\varepsilon_b(\omega)$, and $\varepsilon_c(\omega)$ in Eq. (2). The real and imaginary parts are shown in blue and red curves, respectively. The optical phonon peaks are marked with frequency labels. As expected for a properly calculated dielectric model, $\varepsilon_2(\omega) \geq 0$ across the whole spectral range for all three crystal axes and $\varepsilon_2(\omega) \approx 0$ for the low frequency range well below the TO phonons.

B. Phonon modes of FePO$_4$

Although heterosite FePO$_4$ crystals were not available in bulk form, we carried out ellipsometric measurements on a LiFePO$_4$ sample treated with bromine solution (Br$_2$/CH$_3$CN) to chemically extract Li ions from the near-surface layers of the sample, providing a reasonable model of a FePO$_4$ crystal. Figures 5(a) and 5(b) show a SEM image of LFP single crystal which has been immersed into the bromine solution. While some facets demonstrate clear signs of reaction, such as small peels and cracks, other facets are left practically intact revealing a strong

10

anisotropy of reactivity of the LFP facets with the bromine solution. Of the (100) and (001) facets of the studied LFP single crystal, only the (001) facet actively reacted with bromine solution providing us with a model of the $FePO_4$ (001) plane.

The $FePO_4$ phonon modes were measured on the (001) plane of the delithiated LFP sample in the spectral range from 450 to 2000 cm^{-1} by means of RAE. The *pseudo*-dielectric functions $\langle \varepsilon(\omega) \rangle$ measured in two experimental configurations $(a \| x, b \| y)$ and $(b \| x, a \| y)$ are shown in Figs. 6(a) and 6(b), respectively. For comparison, the *pseudo*-dielectric functions $\langle \varepsilon(\omega) \rangle$ of $LiFePO_4$ sample measured in $a \| x$ and $b \| x$ configurations are also shown in Figs. 6(a) and 6(b), respectively. Preliminary fit of the dielectric response from the delithiated *ab*-surface allowed us to estimate the changes of the phonon mode frequencies upon delithiation. The biggest difference between LFP and FP samples is observed for the high frequency phonons above 800 cm^{-1} associated with vibrations of PO_4 anion groups. The frequency of the strong B_{3u} mode polarized along the *a*-axis is blue-shifted by 72 cm^{-1} from 1028 to 1100 cm^{-1} upon delithiation [see Fig.6(a)], while the frequency of one of the strong B_{2u} modes polarized along the *b*-axis is red-shifted by 21 cm^{-1} from 930 to 909 cm^{-1} [see Fig.6(b)]. Also, the oscillator strength of the weak B_{3u} phonon positioned at 946 cm^{-1} increased from 0.005 to 0.09 while its frequency upshifted by 8 cm^{-1} in delithiated sample as compared to LFP [see Fig.6(a)]. For the lower-frequency phonons (between 450 and 800 cm^{-1}) the largest changes are observed for the modes at ~550 cm^{-1}. The B_{3u} mode at 572 cm^{-1} broadens by a factor of 2 and downshifts by 10 cm^{-1} upon Li removal [see Fig.6(a)] while the B_{2u} mode at 543 cm^{-1} also broadens and downshifts by 22 cm^{-1} [see Fig.6(b)]. We note that due to the absence of the experimental data for the dielectric response from the *c*-axis of the delithiated sample our preliminary fit of the FP sample cannot properly model features originating from the *c*-axis LO frequencies. In particular there is a possibility that the strong feature at 1100 cm^{-1} in the spectra of the FP sample in Fig. 6(a) stems from the *c*-axis LO frequency while the *a*-axis phonon is responsible for the shoulder at ~1070 cm^{-1}. To answer these questions additional experimental data for the *c*-axis dielectric response of delithiated sample is required in the future.

C. DFT phonon calculations

The TO phonon mode frequencies and oscillator strengths computed by solid-state hybrid DFT are presented for the fully optimized and fixed 300 K experimental cell (with optimized atomic positions) structures of LiFePO$_4$ in Table I. The fractions (%) of the mode eigenvectors corresponding to external (*ext*; i.e. rigid) motions of the FeO$_6$, PO$_4$ and LiO$_6$ units are also shown for the fully optimized case, providing a convenient classification of the modes. Where modes are strongly internal (*int*; i.e. unit distortive), the atomic species dominating the motion are also shown where such an attribution can be clearly made. A general crossover might be expected from *ext* dominated motions at low frequency to *int* motions at high frequency. This is broadly borne out, save for the Li rattling motions, which are strongly internal but appear at low frequencies, suggesting that Li ions are rather loosely bound in the crystal, likely confined by spatially complex and significantly anharmonic potentials. Evidence for this also comes from the computed oscillator strengths, which tend to show larger structural sensitivity for the Li rattling modes. Given that the dynamical charge tensors obtained from the fixed cell and fully optimized phonon calculations do not vary significantly, this suggests that the eigenvectors of the rattling modes show acute sensitivity to rather small changes in crystal structure. More generally, the phonon frequencies of the fully optimized structure are higher than those computed using the fixed experimental cell by an average of 11.6 cm^{-1} across all three axes. This can be straightforwardly understood as being due to the small volume contraction in the fully optimized lattice, amounting to 2.3 % of the 300 K experimental value of 291.76 Å^3, leading to slightly stiffer bonds and higher vibrational frequencies.

Turning to examine the phonon parameters in detail, for the B_{3u} symmetry phonons polarized along the *a*-axis, the main discrepancy in oscillator strength between calculations and experiment occurs for the modes at 242 and 345 cm^{-1}. For the first of these, a predominantly Li rattling mode, the fixed cell calculated *S* value underestimates experiment by 0.92 (where oscillator strengths are dimensionless), and the discrepancy worsens with use of the fully optimized structure. Meanwhile, the experimental 345 cm^{-1} mode is assigned to the calculated 304 and 370 cm^{-1} phonons, and the sum of the calculated *S* values, at 0.63, significantly overestimates the experimental value of *S* = 0.05. Neither of the calculated *S* values shows appreciable structural sensitivity. The weak 370 cm^{-1} mode comprises predominantly Li rattling motions, while the eigenvector of the stronger 304 cm^{-1} mode is more complex, involving significant external and internal contributions. The *S* value of 0.29 for the experimental 484 cm^{-1}

12

mode is in good agreement with the sum 0.28 for the assigned calculated 459 and 522 cm^{-1} modes, and, again, neither of the component values changes much with structure.

Examining the B_{2u} symmetry phonons polarized along the b-axis, the main discrepancy arises for the low frequency 194 cm^{-1} mode, where the calculated S value exceeds experiment by 1.44, although agreement does improve slightly with the use of the optimized cell, bringing the overestimate down to 1.11. The S values of the experimental modes at 346 and 420 cm^{-1} are significantly under- and overestimated, respectively, by the DFT calculation, but the total oscillator strength in this spectral region is in good agreement at $S = 0.74$ from experiment and $S = 1.04$ from the calculation. Neither of the DFT S values shows appreciable structural sensitivity.

Finally, for the B_{1u} symmetry phonons polarized along the c–axis, the main discrepancy arises for the experimental 229 cm^{-1} mode, where the calculated S value overestimates experiment by 1.96. However, this mode shows a very large structural sensitivity, where use of the optimized cell brings the overestimate down to 0.91. Another significant difference arises for the experimental 189 cm^{-1} mode, where the calculated S value underestimates experiment by 0.94, although use of the optimized cell again improves agreement, bringing the underestimate down to 0.76. The 260 cm^{-1} mode also shows strong structural sensitivity, with a difference in S value of 0.61 between fixed and optimized cells. No mode comparable to the experimental 372 cm^{-1} phonon arises from the calculation, although we note this is a broad spectral feature, while the calculated 950 cm^{-1} mode is absent from the experimental spectrum, in keeping with its vanishing oscillator strength. The experimental 631 cm^{-1} mode is assigned to a combination of the calculated 582 and 650 cm^{-1} modes, with a total oscillator strength dominated by the latter phonon.

The obtained agreement between our experimental $\omega_{i,\mathrm{exp}}$ and calculated $\omega_{i,\mathrm{th}}$ values for all phonon frequencies can be summarized by the average relative difference parameter $\delta = \left(K + L + N\right)^{-1} \sum\limits_{i=1}^{K+L+N} \left|\omega_{i,\mathrm{th}} - \omega_{i,\mathrm{exp}}\right| \big/ \omega_{i,\mathrm{exp}}$ that is equal to 0.051 for the experimental cell and 0.068 for the optimized cell approaches for LiFePO$_4$ crystal. Although this agreement is not perfect, we consider this result acceptable taking into account the nontrivial behavior of Li in the LiFePO$_4$ crystal lattice, such as its rather weak bounding to the crystal and a significant

anharmonicity of Li crystal potentials. Several approaches may be implemented in the future to improve the agreement between theory and experiment. One of them is to measure Raman-active phonons and compare both Raman- and IR-active phonons to the corresponding DFT results. Another approach would be to account for the antiferromagnetic (AFM) ordering of Fe^{2+} spins along b in the $LiFePO_4$ [31]. Recently this approach has been successfully implemented in Ref. [20] for theoretical analysis of the phonons in inelastic neutron scattering experiments in $LiFePO_4$ polycrystals.

The DFT calculations qualitatively reproduce the effects of delithiation to $FePO_4$ on the spectra. The TO phonon mode frequencies and oscillator strengths computed for the fully optimized and fixed 300 K experimental cell (with optimized atomic positions) structures of $FePO_4$ are shown in Table II. For the high frequency phonons, the strong experimental B_{3u} mode at 1028 cm^{-1} is blueshifted on delithiation by 48 and 18 cm^{-1} in the fixed experimental cell and fully optimized calculations, respectively, as compared with an experimental blueshift of 72 cm^{-1}. The strong experimental B_{2u} mode at 930 cm^{-1} is redshifted on delithiation by 22 and 33 cm^{-1} in the fixed experimental cell and fully optimized calculations, respectively, as compared with an experimental redshift of 21 cm^{-1}. The weak experimental B_{3u} mode at 946 cm^{-1} is blueshifted on delithiation by 25 and 11 cm^{-1} in the fixed experimental cell and fully optimized calculations, respectively, as compared with an experimental blueshift of 8 cm^{-1}. Also, the calculations accurately reproduce the increase in oscillator strength from 0.003 to 0.09 on delithiation in both structures, as compared with an experimental increase from 0.005 to 0.09. For lower frequency phonons, the redshift of the experimental B_{3u} mode at 572 cm^{-1} on delithiation is overestimated at 51 and 62 cm^{-1} in the fixed experimental cell and fully optimized calculations, respectively, as compared with an experimental redshift of 10 cm^{-1}. Finally, the weak experimental B_{2u} mode at 543 cm^{-1} is redshifted on delithiation by 33 and 34 cm^{-1} in the fixed experimental cell and fully optimized calculations, respectively, as compared with an experimental redshift of 22 cm^{-1}. The comparison of experimental and calculated changes to phonon mode frequencies upon delithiation of the ab-surface of the LFP sample is summarized in Table III.

IV. CONCLUSIONS

We report the first study of the optical phonons in $LiFePO_4$ oriented single crystals. The majority of the optical phonons have been identified for three orthorhombic a, b, and c axes. The

phonon modes of a chemically delithiated $FePO_4$ sample were also measured along the *a* and *b* axes. The biggest difference between $LiFePO_4$ and $FePO_4$ samples was observed for the high frequency phonons above 800 cm^{-1}, which are related to distortive vibrations in the PO_4 anion units. Good agreement was found between the experimental data and the results of solid-state hybrid DFT calculations for the phonon modes in both $LiFePO_4$ and $FePO_4$. The experimental and theoretical data presented here will be useful for further analysis of the Li (de)intercalation process as well as for future studies of the phonon spectra in a broad class of Li-based materials for rechargeable battery applications.

TABLE I. Experimental and calculated (both experimental and optimized cells) parameters for TO phonons polarized along the *a*, *b*, and *c* axes for LiFePO$_4$, *T*=300 K. The phonon frequency ω_0 and broadening γ are in cm^{-1}, the oscillator strength *S* is in units of ε_∞. The fractions (%) of the mode eigenvectors corresponding to external (*ext*; i.e. rigid) motions of the FeO$_6$, PO$_4$ and LiO$_6$ units are shown for the fully optimized case. The experimental and calculated values for ε_∞ and quasi-static $\varepsilon(0)$ are listed at the bottom for all three axes.

Mode		Experiment			Theory (expt. cell)		Theory (opt. cell)			Theory mode description (int dominant species)
		ω_0	γ	S	ω_0	S	External	ω_0	S	
a	1	141	2.8	0.15	154	0.28	83.4	160	0.23	LiO$_6$ ext
(*B$_{3u}$*)	2	176	4.1	0.09	195	0.09	36.3	204	0.10	FeO$_6$ int (Fe)
	3	242	19.7	3.8	242	2.88	11.9	265	2.56	LiO$_6$ int (Li)
	4	262	4.4	0.18	271	0.40	18.8	288	0.13	LiO$_6$ int (Li)
	5	345	13.7	0.05	304	0.57	43.1	316	0.52	LiO$_6$ ext int
	6				370	0.06	14.6	378	0.09	LiO$_6$ int (Li)
	7	484	47	0.29	459	0.21	10.3	483	0.23	LiO$_6$ int (Li)
	8				522	0.07	5.9	530	0.08	LiO$_6$ int (O)
	9	572	11.3	0.2	590	0.14	12.6	596	0.13	LiO$_6$ PO$_4$ int (O)
	10	645	7.1	0.08	672	0.07	9.7	679	0.08	LiO$_6$ FeO$_6$ PO$_4$ int (O)
	11	946	4.8	0.005	951	0.00	5.8	960	0.00	FeO$_6$ LiO$_6$ PO$_4$ int (O)
	12	1028	10.8	0.48	1042	0.47	17.6	1052	0.47	PO$_4$ int (P O)
	13	1094	6.2	0.014	1116	0.02	23.0	1128	0.01	PO$_4$ int (P O)
b	1	194	3.9	1.15	153	2.59	14.5	174	2.26	LiO$_6$ int (Li)
(*B$_{2u}$*)	2	205	8.6	0.19	202	0.05	7.8	234	0.24	LiO$_6$ int (Li)
	3	220	14.4	0.79	215	0.72	48.9	216	0.37	LiO$_6$ ext int (Li)
	4	246	6.7	0.3	273	0.41	35.5	277	0.31	LiO$_6$ int (Li)
	5	346	12.8	0.44	378	0.28	32.6	389	0.22	LiO$_6$ int (O)
	6	420	33.7	0.3	412	0.76	6.5	439	0.74	LiO$_6$ int (Li)
	7	462	18.5	0.41	488	0.32	18.5	498	0.37	FeO$_6$ LiO$_6$ int (O)
	8	543	6.5	0.22	551	0.14	24.8	554	0.13	PO$_4$ LiO$_6$ int (O)
	9	930	15.7	0.73	955	0.67	26.9	963	0.68	PO$_4$ int (P O)
c	1	176	3.0	0.05	188	0.01	33.0	195	0.03	LiO$_6$ FeO$_6$ int (Li Fe)
(*B$_{1u}$*)	2	189	4.4	1.1	215	0.16	64.2	226	0.34	LiO$_6$ ext
	3	229	7.3	0.37	241	2.33	20.3	261	1.28	LiO$_6$ int (Li)
	4	260	10.7	0.5	250	0.03	64.3	262	0.64	LiO$_6$ ext
	5	298	14.6	0.16	309	0.24	12.2	319	0.11	LiO$_6$ int (Li)
	6	353	13.8	0.76	368	1.05	17.3	381	0.98	LiO$_6$ int (Li)
		372	35.2	0.84						
	7	495	26.8	0.4	471	0.51	9.3	494	0.51	LiO$_6$ int (Li)
	8	509	17.5	0.09	507	0.12	8.3	517	0.16	LiO$_6$ FeO$_6$ PO$_4$ int (O)
	9				582	0.01	11.3	588	0.02	LiO$_6$ FeO$_6$ int (O)
	10	631	8.7	0.16	650	0.17	11.9	657	0.17	LiO$_6$ int (O Li)
	11				950	0.00	12.9	959	0.00	LiO$_6$ FeO$_6$ PO$_4$ int (O)
	12	1073	15.1	0.32	1093	0.35	19.8	1104	0.35	PO$_4$ int (P O)
	13	1158	14	0.02	1158	0.03	20.2	1168	0.04	PO$_4$ int (P)

Experiment: $\varepsilon_{\infty,a} \approx \varepsilon_{\infty,b} \approx \varepsilon_{\infty,c} \approx 2.8$ $\varepsilon_a(0)=8.1,\ \varepsilon_b(0)=7.3,\ \varepsilon_c(0)=7.6$

Theory (expt. cell): $\varepsilon_{\infty,a}=2.5,\ \varepsilon_{\infty,b}=2.6, \varepsilon_{\infty,c}=2.5$ $\varepsilon_a(0)=7.8,\ \varepsilon_b(0)=8.6,\ \varepsilon_c(0)=7.6$

Theory (opt. cell): $\varepsilon_{\infty,a}=2.6,\ \varepsilon_{\infty,b}=2.6, \varepsilon_{\infty,c}=2.6$ $\varepsilon_a(0)=7.2,\ \varepsilon_b(0)=7.9,\ \varepsilon_c(0)=7.2$

TABLE II. Calculated (both experimental and optimized cells) parameters for TO phonons polarized along the *a, b* and *c* axes for FePO$_4$, *T*=300 K. The phonon frequency ω_0 is in cm^{-1}, the oscillator strength *S* is in units of ε_∞. The fractions (%) of the mode eigenvectors corresponding to external (*ext*; i.e. rigid) motions of the FeO$_6$ and PO$_4$ units are shown for the fully optimized case.

Mode		Theory (expt. cell)			Theory (opt. cell)		Theory mode description (int dominant species)
		ω_0	S	External	ω_0	S	
a	1	190	0.16	73.7	184	0.14	PO$_4$ ext
(*B$_{3u}$*)	2	263	0.04	50.7	262	0.07	FeO$_6$ PO$_4$ ext int (Fe O)
	3	346	0.00	48.9	333	0.00	FeO$_6$ PO$_4$ ext int (O)
	4	386	3.05	49.4	383	3.09	FeO$_6$ PO$_4$ ext int (O)
	5	539	0.40	4.1	534	0.35	FeO$_6$ PO$_4$ int (O)
	6	628	0.00	9.8	623	0.00	FeO$_6$ PO$_4$ int (O)
	7	698	0.27	13.4	694	0.28	FeO$_6$ PO$_4$ int (P O)
	8	976	0.09	4.6	971	0.09	FeO$_6$ PO$_4$ int (O)
	9	1090	0.99	11.7	1070	1.08	FeO$_6$ PO$_4$ int (P O)
	10	1129	0.14	7.3	1117	0.12	FeO$_6$ PO$_4$ int (O)
b	1	203	7.12	49.9	198	7.47	FeO$_6$ PO$_4$ ext int (Fe O)
(*B$_{2u}$*)	2	284	0.01	44.7	276	0.00	FeO$_6$ PO$_4$ ext int (O)
	3	341	0.49	60.5	326	0.41	FeO$_6$ PO$_4$ ext
	4	443	0.24	29.3	430	0.23	FeO$_6$ PO$_4$ int (O)
	5	518	0.82	13.9	520	0.74	FeO$_6$ PO$_4$ int (O)
	6	933	0.84	25.6	930	0.78	FeO$_6$ PO$_4$ int (P O)
c	1	199	0.94	73.4	197	0.92	FeO$_6$ PO$_4$ ext
(*B$_{1u}$*)	2	254	1.72	65.8	252	1.88	FeO$_6$ PO$_4$ ext
	3	341	0.10	53.1	334	0.13	FeO$_6$ PO$_4$ ext int (O)
	4	419	0.67	54.2	408	0.64	FeO$_6$ PO$_4$ ext int (O)
	5	547	0.49	12.5	538	0.48	FeO$_6$ PO$_4$ int (O)
	6	593	0.09	6.5	592	0.09	FeO$_6$ PO$_4$ int (O)
	7	661	0.38	12.0	658	0.35	FeO$_6$ PO$_4$ int (O)
	8	981	0.06	10.0	976	0.06	FeO$_6$ PO$_4$ int (P O)
	9	1087	0.65	12.7	1074	0.67	FeO$_6$ PO$_4$ int (P O)
	10	1271	0.01	8.2	1258	0.01	FeO$_6$ PO$_4$ int (P O)

Theory (expt. cell): $\varepsilon_{\infty,a}=3.9, \varepsilon_{\infty,b}=3.4, \varepsilon_{\infty,c}=3.5$ $\varepsilon_a(0)=9.0, \varepsilon_b(0)=12.9, \varepsilon_c(0)=8.6$

Theory (opt. cell): $\varepsilon_{\infty,a}=3.9, \varepsilon_{\infty,b}=3.4, \varepsilon_{\infty,c}=3.5$ $\varepsilon_a(0)=9.1, \varepsilon_b(0)=13.0, \varepsilon_c(0)=8.7$

18

TABLE III. Experimental and calculated changes to phonon frequencies of the LiFePO$_4$ crystal upon delithiation of the ab-surface. Phonon frequencies are in cm^{-1}. Δ is a difference between phonon frequencies in FePO$_4$ (FP) and LiFePO$_4$ (LFP) samples.

Mode	Experiment			Theory (expt. cell)			Theory (opt. cell)		
	LFP	FP	Δ	LFP	FP	Δ	LFP	FP	Δ
a	572	562	-10	590	539	-51	596	534	-62
(B_{3u})	946	954	8	951	976	25	960	971	11
	1028	1100	72	1042	1090	48	1052	1070	18
b	543	521	-22	551	518	-33	554	520	-34
(B_{2u})	930	909	-21	955	933	-22	963	930	-33
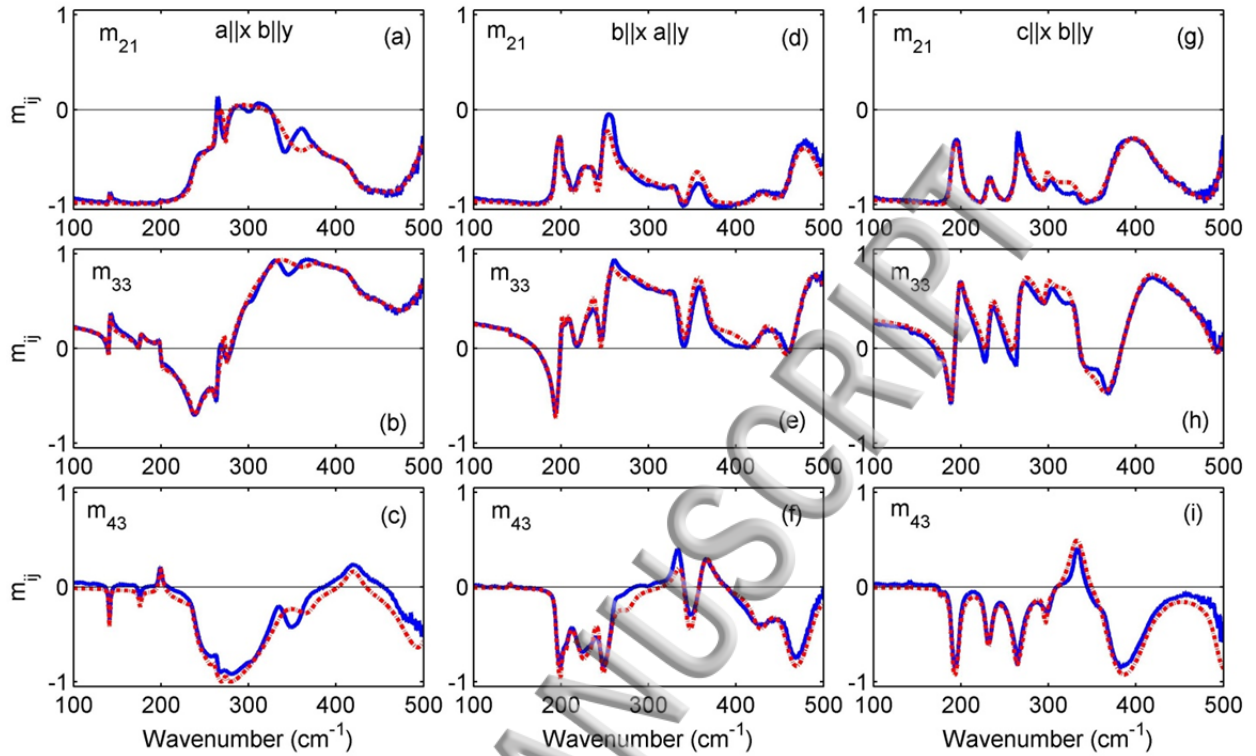
FIG. 1. Spectra of the normalized Mueller matrix components $m_{12}(\omega)$, $m_{33}(\omega)$, and $m_{43}(\omega)$ (blue curves) for LiFePO$_4$ crystals measured using RCE at T=300 K in three experimental configurations: (a,b,c) $a \parallel x$ and $b \parallel y$; (d,e,f) $b \parallel x$ and $a \parallel y$; (g,h,i) $c \parallel x$ and $b \parallel y$. The results of the fit using Eq. (2) for the parametric description model of the anisotropic dielectric function are shown with dash-dot red curves.
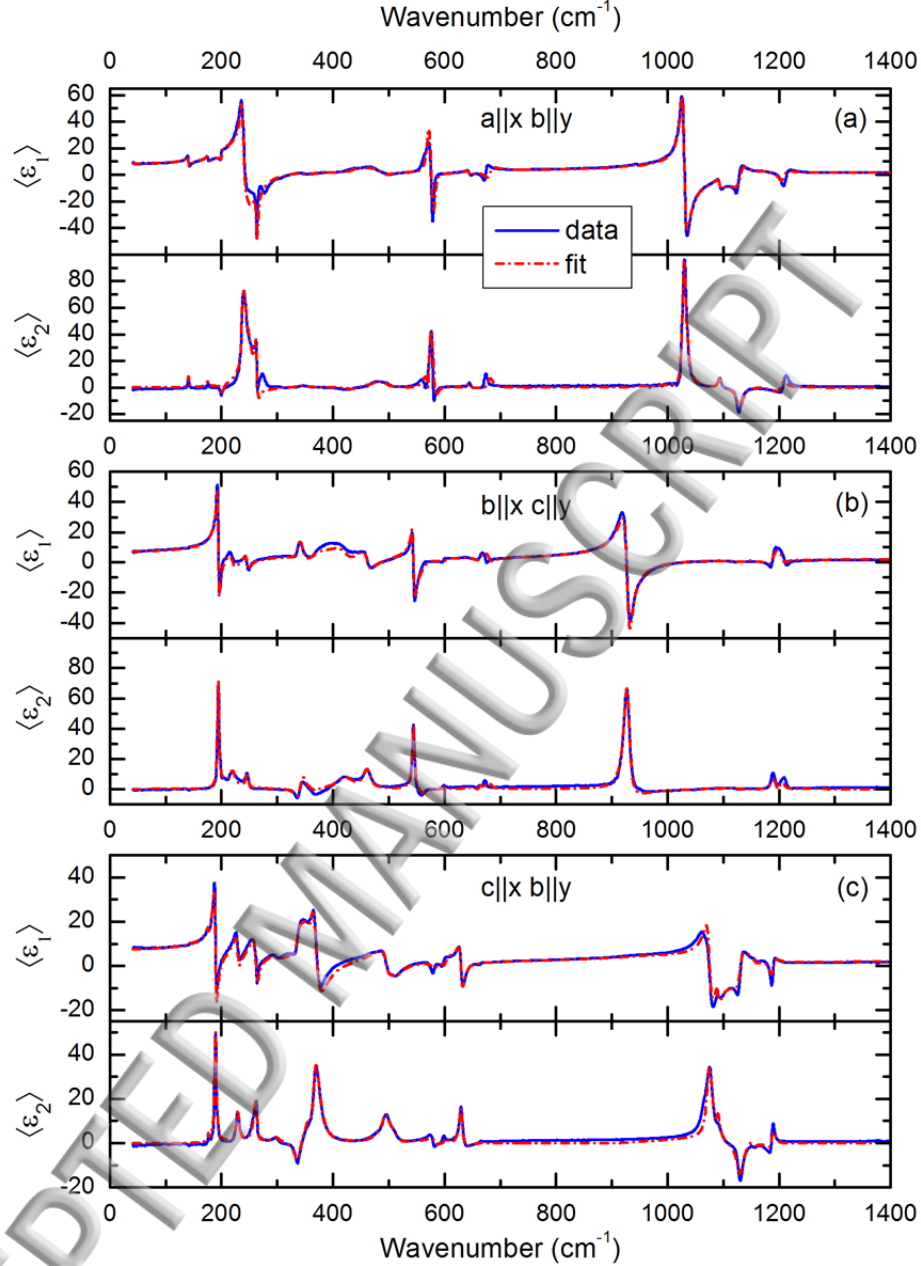
FIG. 2. Spectra of the real $\langle\varepsilon_1(\omega)\rangle$ and imaginary $\langle\varepsilon_2(\omega)\rangle$ components of the *pseudo*-dielectric function measured for LiFePO$_4$ crystals at T=300 K in three experimental configurations: (a) $a\parallel x$ and $b\parallel y$, (b) $b\parallel x$ and $a\parallel y$, (c) $c\parallel x$ and $b\parallel y$ (blue solid curves). Strong peaks correspond to optical phonons. The spectral range between 50 cm^{-1} and 450 cm^{-1} is measured using RCE, while the spectral range above 450 cm^{-1} is measured with RAE. The results of the fit using Eq. (2) for the parametric description model of the anisotropic dielectric function are shown with dash-dot red curves.
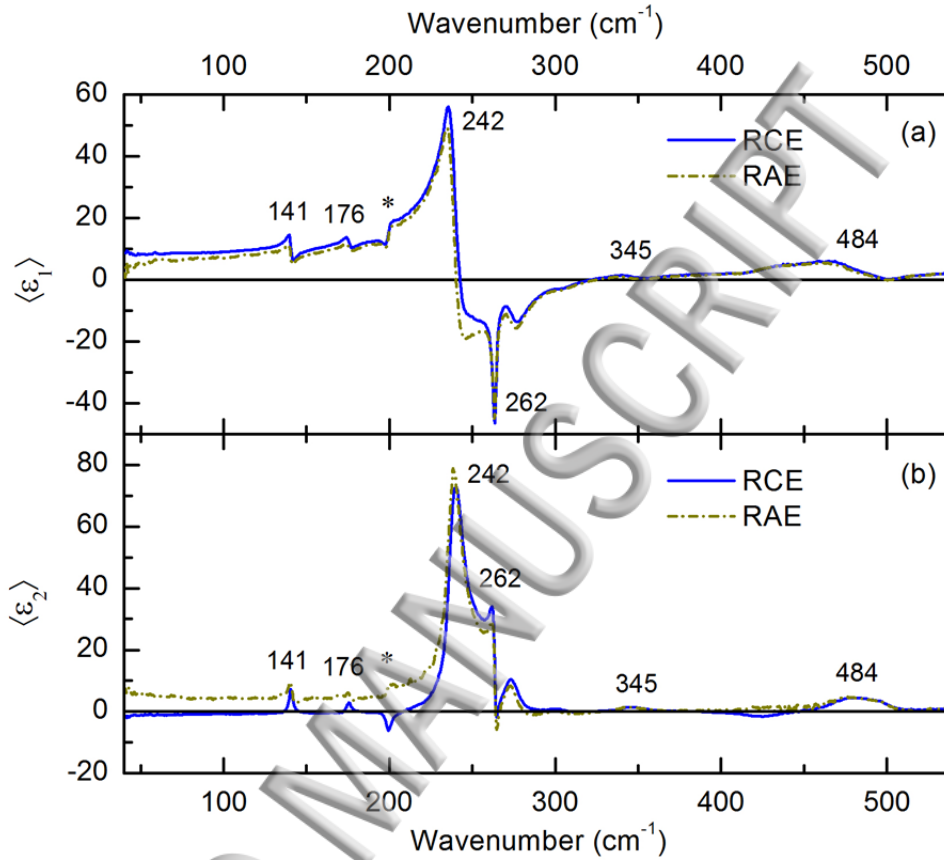
FIG. 3. (a) Real and (b) imaginary parts of the *pseudo*-dielectric function for LiFePO$_4$ crystal measured with RCE (blue solid curve) and RAE (brown dashed curves) for $a \parallel x$ and $b \parallel y$. The optical phonon peaks polarized along the a axis are marked with wavenumber labels. Note the difference between two spectra below 230 cm^{-1}. The spectral feature that originates from a phonon at ~200 cm^{-1}, which is polarized along the b axis, is marked with an asterisk.
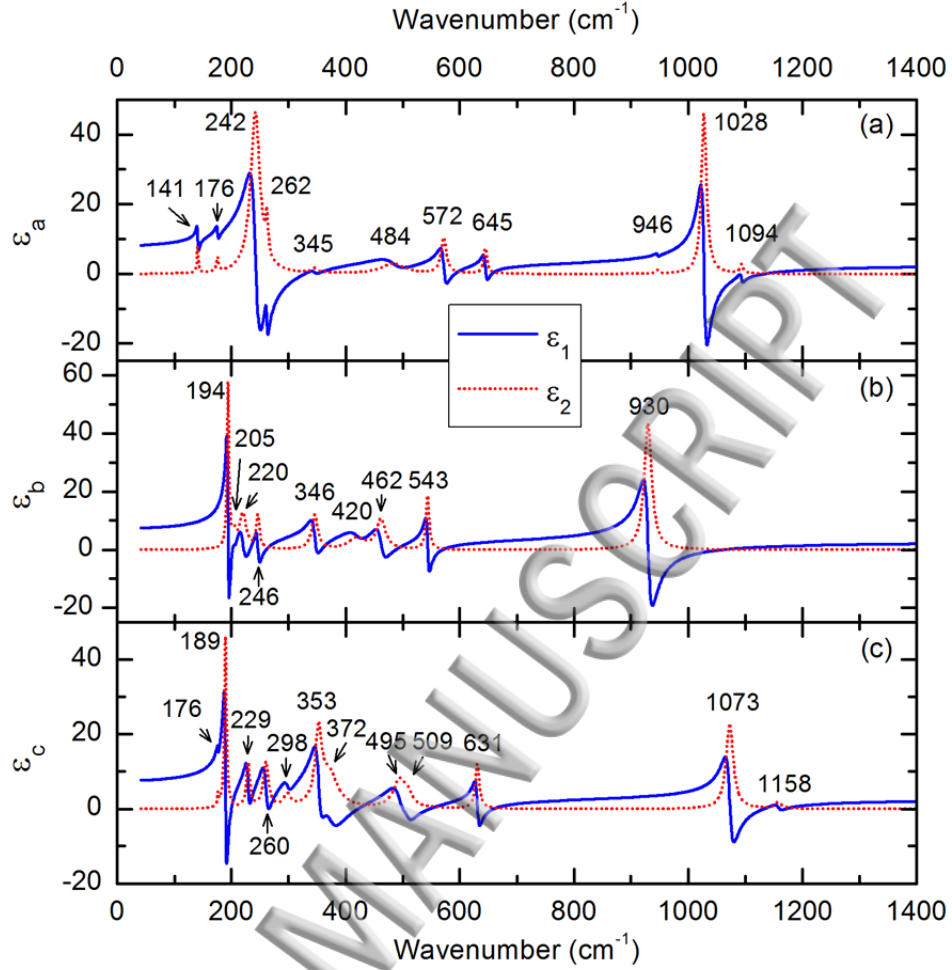
FIG. 4. Spectra of real (blue solid curves) and imaginary (red dotted curves) parts of diagonal components (a) $\varepsilon_a(\omega)$, (b) $\varepsilon_b(\omega)$, and (c) $\varepsilon_c(\omega)$ of the dielectric function tensor $\hat{\varepsilon}(\omega)$ of LiFePO$_4$ calculated using the experimental phonon parameters from Table I. The optical phonon peaks are marked with wavenumber labels.
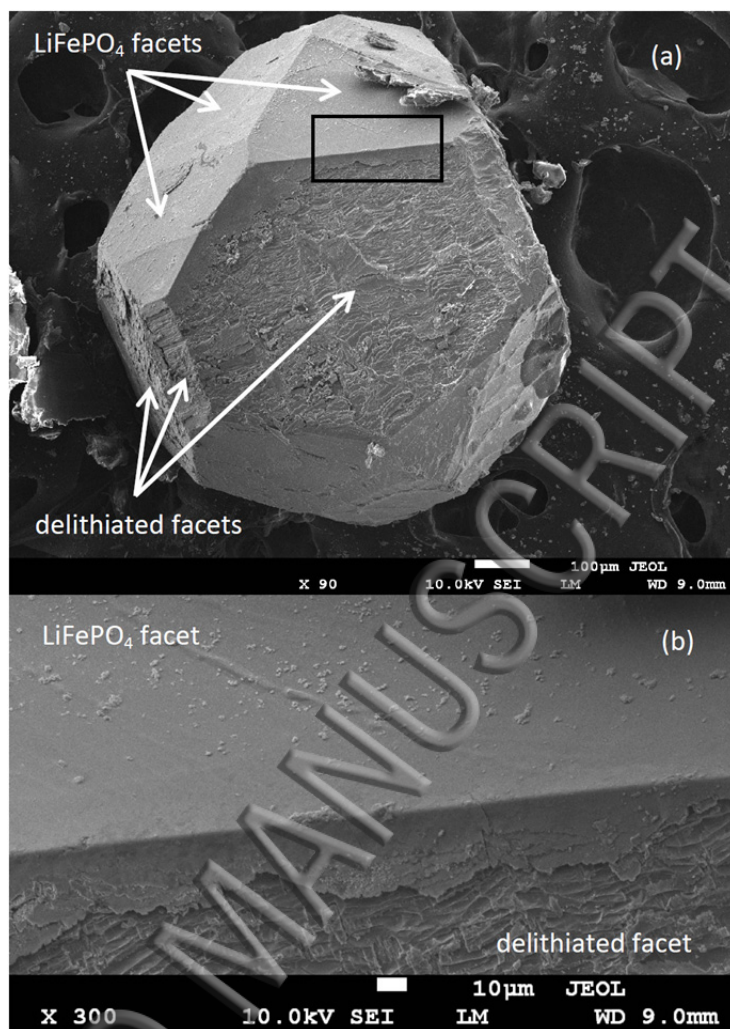
FIG. 5. (a) SEM image of a LiFePO$_4$ single crystal which undergone delithiation process by being immersed into the bromine solution Br$_2$/CH$_3$CN. While some facets of the sample actively reacted with the bromine solution as evidenced by small peels and cracks on the surface, other facets are left practically intact implying high anisotropy of the effectiveness of chemical delithiation of LiFePO$_4$ facets. (b) Zoom of rectangular region in (a), showing the boundary between high and low reactivity facets.
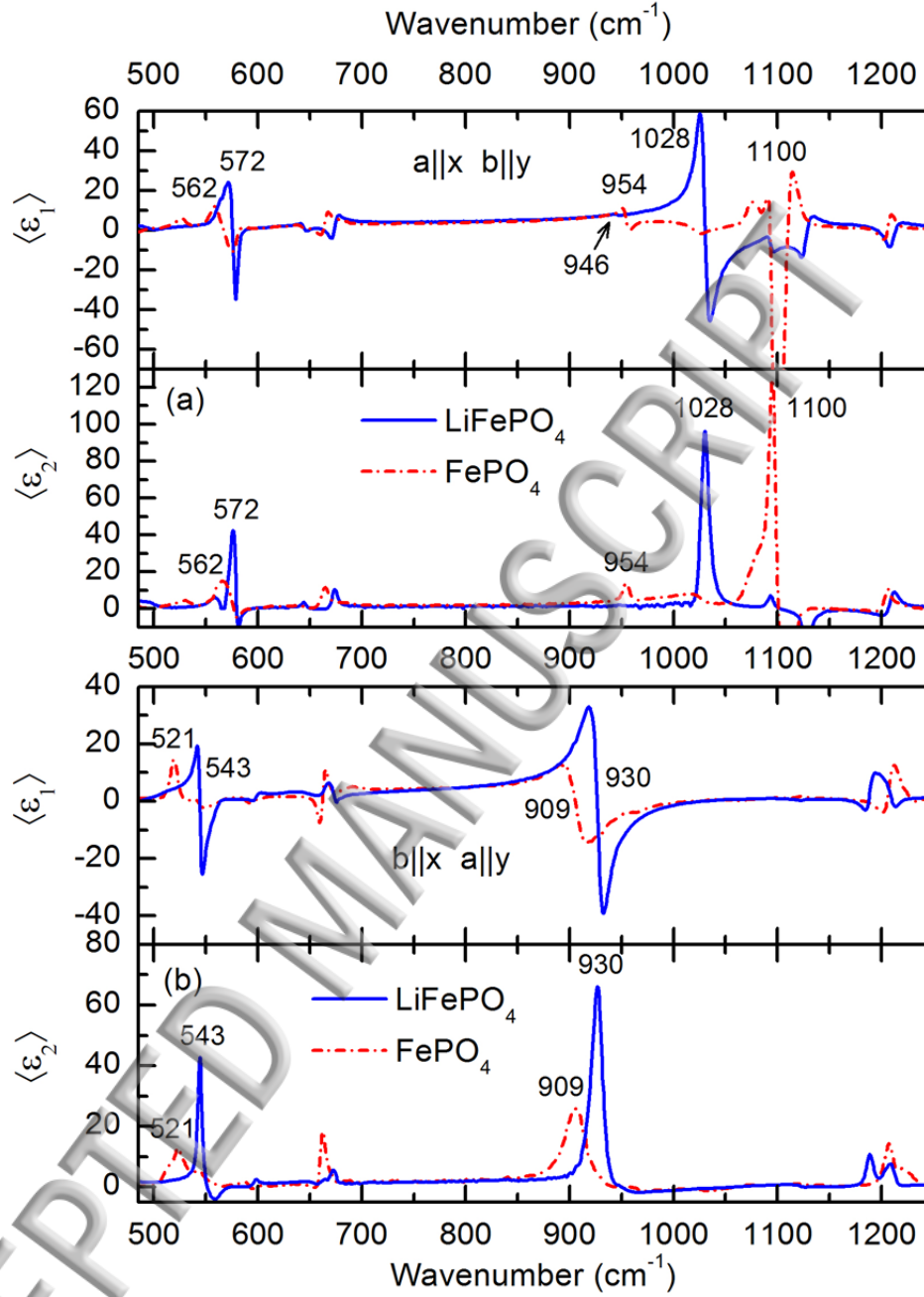
FIG. 6. Spectra of real $\langle \varepsilon_1(\omega) \rangle$ and imaginary $\langle \varepsilon_2(\omega) \rangle$ components of the *pseudo*-dielectric function measured for LiFePO$_4$ (solid blue line) and heterosite FePO$_4$ (dash-dot red line) crystals at $T=300$ K in two experimental configurations: (a) $a \parallel x$ and $b \parallel y$, (b) $b \parallel x$ and $a \parallel y$.

REFERENCES

[1] A. K. Padhi, K. S. Nanjundaswamy, and J. B. Goodenough, J. Electrochem. Soc. **144**, 1198 (1997)

[2] A. Yamada, S. C. Chung, and K. Hinokuma, J. Electrochem. Soc. **148**, A224 (2001).

[3] A. S. Andersson, J. O. Thomas, B. Kalska, and L. Häggström, Electrochem. Solid-State Lett. **3**, 66 (2000).

[4] B. L. Ellis, K. T. Lee, and L. F. Nazar, Chem. Mater. **22**, 691 (2010).

[5] J.-M. Tarascon and M. Armand, Nature **414**, 359 (2001).

[6] H. Huang, S.-C. Yin, and L. F. Nazar, Electrochem. Solid-State Lett. **4**, A170 (2001).

[7] M. Stanley Whittingham, Chem. Rev. **114**, 11414 (2014).

[8] L. Laffont, C. Delacourt, P. Gibot, M. Yue Wu, P. Kooyman, C. Masquelier, and J. Marie Tarascon, Chem. Mater. **18**, 5520 (2006).

[9] C. Delmas, M. Maccario, L. Croguennec, F. Le Cras, F. Weill, Nat. Mater. **7**, 665 (2008).

[10] G. Chen, X. Song, T. Richardson, J. Electrochem. Solid-State Lett. **9**, A295 (2006).

[11] R. Malik, F. Zhou and G. Ceder, Nat. Mater. **10**, 587 (2011).

[12] A. Van der Ven, J. C. Thomas, Q. Xu, B. Swoboda, and D. Morgan, Phys. Rev. B **78**, 104306 (2008).

[13] I. T. Lucas, A. S. McLeod, J. S. Syzdek, D. S. Middlemiss, C. P. Grey, D. N. Basov, and R. Kostecki, Nano Lett. **15**, 1 (2015).

[14] M. Th. Paques-Ledent and P. Tarte, Spectrochim. Acta **30A**, 673 (1974).

[15] Christopher M. Burba and Roger Frech, J. Electrochem. Soc. **151**, A1032 (2004).

[16] W. Paraguassu, P. Freire, V. Lemos, S. Lala, L. Montoro and J. Rosolen, J. Raman Spectrosc. **36**, 213 (2005).

[17] J. Wu, G. K. P. Dathar, C. Sun, M. G. Theivanayagam, D. Applestone, A. G. Dylla, A. Manthiram, G. Henkelman, J. B. Goodenough and K. J. Stevenson, Nanotechnology **24**, 424009 (2013).

[18] S. Q. Shi, H. Zhang, X. Z. Ke, C. Y. Ouyang, M. S. Lei and L. Q. Chen, Phys. Lett. A **373**, 4096 (2009).

[19] S. L. Shang, Y. Wang, Z. G. Mei, X. D. Hui and Z. K. Liu, J. Mater. Chem. **22**, 1142 (2012).

[20] P. Goel, M. K. Gupta, R. Mittal, S. Rols, S. J. Patwe, S. N. Achary, A. K. Tyagi and S. L. Chaplot, J. Mater. Chem. A **2**, 14729 (2014).

[21] Y. Janssen, D. Santhanagopalan, D. Qian, M. Chi, X. Wang, C. Hoffmann, Y. S. Meng, and P. G. Khalifah, Chem. Mater. **25**, 4574 (2013)

[22] T. N. Stanislavchuk, T. D. Kang, P. D. Rogers, E. C. Standard, R. Basistyy, A. M. Kotelyanskii, G. Nita, T. Zhou, G. L. Carr, M. Kotelyanskii, and A. A. Sirenko, Rev. Sci. Instr. **84**, 023901 (2013).

[23] T. D. Kang, E. Standard, G. L. Carr, T. Zhou, M. Kotelyanskii, and A. A. Sirenko, Thin Solid Films **519**, 2698 (2011).

[24] H. Fujiwara, *Spectroscopic Ellipsometry: Principles and Applications* (John Wiley & Sons, 2007).

[25] R. Dovesi, R. Orlando, B. Civalleri, C. Roetti, V. R. Saunders, C. M. Zicovich-Wilson, Zeitschrift Fur Kristallographie **220**, 571 (2005).

[26] R. Dovesi, V. R. Saunders, C. Roetti, R. Orlando, C. M. Zicovich-Wilson, F. Pascale, B. Civalleri, K. Doll, N. M. Harrison, I. J. Bush, P. D'Arco, M. Llunell, *CRYSTAL09 User's Manual* (University of Torino, Torino, 2009).

[27] CRYSTAL09 online basis set repository at www.crystal.unito.it

[28] A. D. Becke, J. Chem. Phys. **98**, 5648 (1993).

[29] C. Lee, W. Yang, and R. Parr, Phys. Rev. B **37**, 785 (1988).

[30] B. Miehlich, A. Savin, H. Stoll, and H. Preuss, Chem. Phys. Lett. **157**, 200 (1989).

[31] R. P. Santoro and R. E. Newnham, Acta Cryst. **22**, 344 (1967).

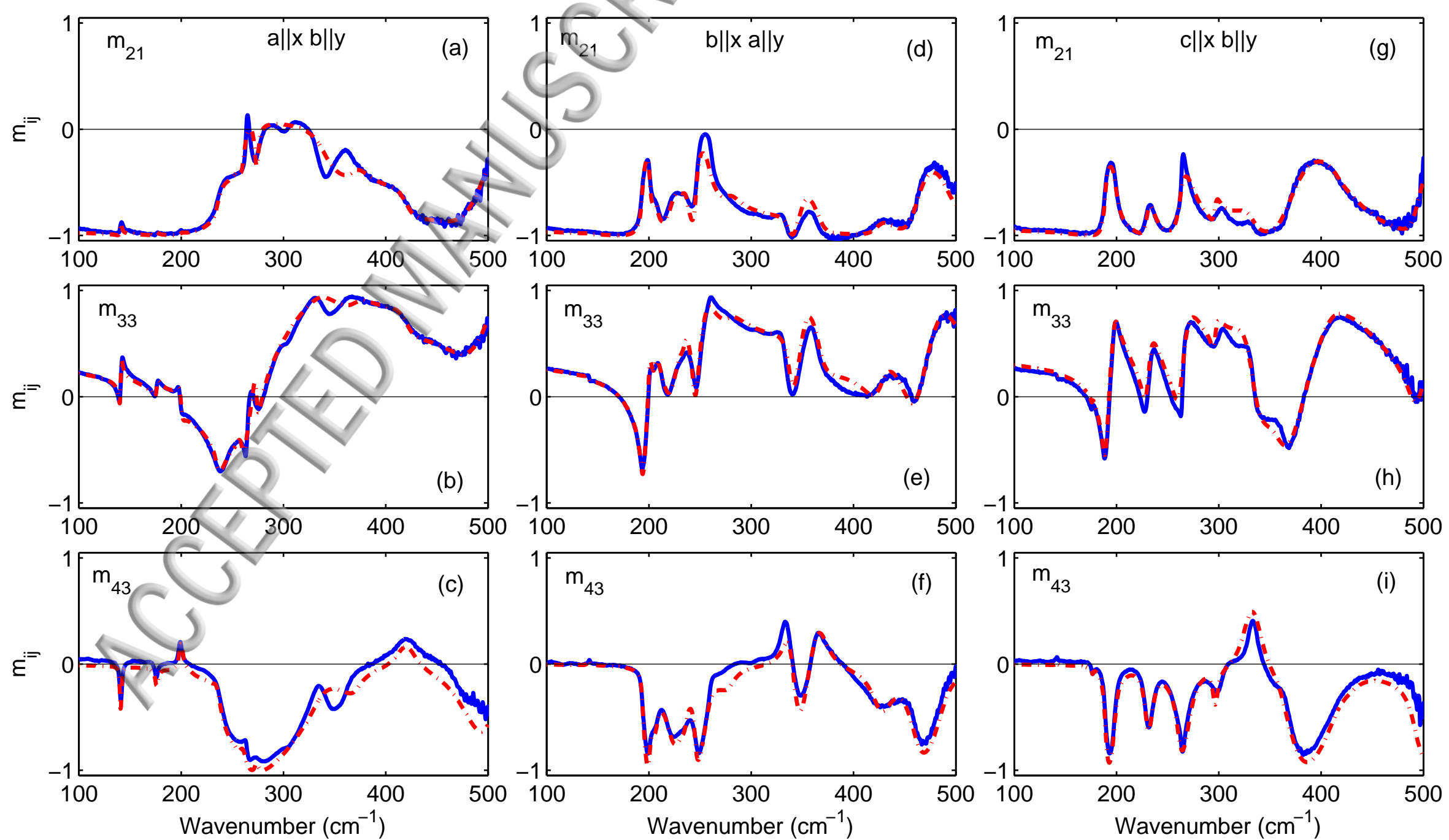[32] G. Rousse, J. Rodriguez-Carvajal, S. Patoux and C. Masquelier, Chem. Mater. **15**, 4082 (2003).

[33] C. M. Zicovich-Wilson, F. Pascale, C. Roetti, V. R. Saunders, R. Orlando, R. Dovesi, J. Comput. Chem. **25**, 1873 (2004).
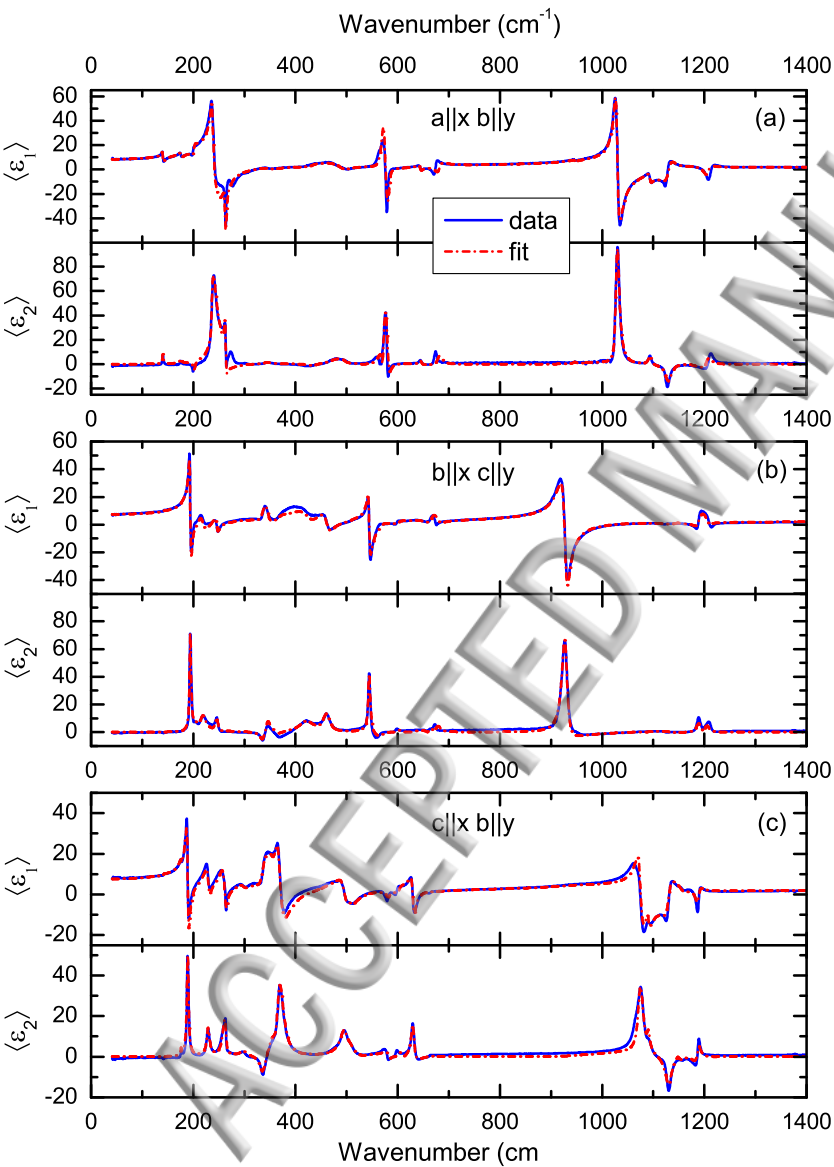
[34] F. Pascale, C. M. Zicovich-Wilson, F. Lopez Gejo, B. Civalleri, R. Orlando, R. Dovesi, J. Comput. Chem. **25**, 888 (2004).

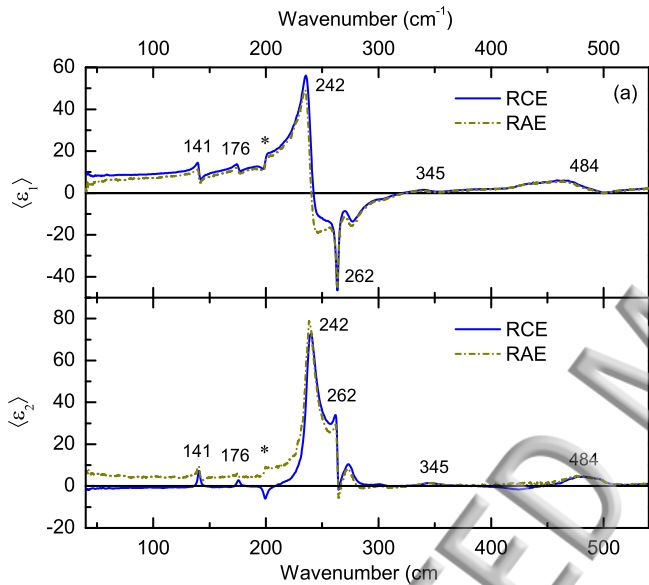[35] M. Born, K. Huang, *Dynamical Theory of Crystal Lattices*, (Oxford University Press, New York, 1988).

[36] C. M. Zicovich-Wilson, R. Dovesi, and V. R. Saunders, J. Chem. Phys. **115**, 9708 (2001).

[37] P. D. Rogers, T. D. Kang, T. Zhou, M. Kotelyanskii, and A. A. Sirenko, Thin Solid Films **519**, 2668 (2011).

Wavenumber (cm⁻¹)

(a)

(a)

LiFePO$_4$ facets

delithiated facets

X 90   10.0kV SEI   LM   WD 9.0mm   100µm JEOL

(b)

LiFePO$_4$ facet

delithiated facet

X 300   10.0kV SEI   LM   WD 9.0mm   10µm JEOL